1 **The influence of Typhoon "Hongxia" on the intrusion of the Kuroshio current into the South**

2 **China Sea**

3 Shumin Gao[1], Shuzong Han[1], Shicheng Wang[1], Mingjie Wang[1], Kejian Wu[1], Lili Liu[2,3]

4 [1] College of Oceanic and Atmospheric Sciences, Ocean University of China, Qingdao, China

5 [2] Tianjin Key Laboratory for Oceanic Meteorology, Tianjin, China

6 [3] Tianjin Institute of Meteorological Science, Tianjin, China

7 Correspondence to: S. Han hansz@ouc.edu.cn

8 **Key Points:** The impact of typhoons on the position and velocity of the Kuroshio axis is assessed. The impact of

9 typhoons on the water, heat and salt fluxes associated with the Kuroshio intrusion in the South China Sea is

10 evaluated. The impact of typhoons on the Kuroshio intrusion and the relevant temperature and salinity in the

11 northeastern South China Sea are analyzed.

12 **Abstract** This paper uses the Coupled Ocean-Atmosphere-Wave-Sediment Transport (COAWST) model to

13 analyze the impact of typhoon "Hongxia" on the velocity and position movement of the Kuroshio axis, the impact

14 of typhoons on the Kuroshio intrusion into South China Sea (SCS), the corresponding water, heat, and salt fluxes,

15 and the impact of Kuroshio water in the northeastern SCS. When typhoon "Hongxia" passed, the Kuroshio

16 intrusion into the SCS was the most significant at 21°N latitude. In the vertical direction, the Kuroshio intrusion

17 was strongest in the subsurface layer, leading to the most significant changes in temperature and salinity in the

18 northeastern part of the SCS in the subsurface layer. Under the influence of the southeastern monsoon in summer, a

19 large amount of low-salinity water accumulates at the surface of the northeastern part of the SCS, and Kuroshio

20 intrusive water remains in the bottom and middle portions of the subsurface layer. The westward deviation of the

21 Kuroshio axis caused by the typhoon displays a certain lag compared with the hot and salty water intrusion into the

22 SCS approximately 7 d later. The impact of the typhoon on the Kuroshio intrusion into the SCS lasts for 20 d. The

23 typhoon caused increases in the water, heat, and salt fluxes associated with the Kuroshio intrusion into the SCS,

24 and the contribution of the typhoon to these fluxes was as high as 40%. Under typhoon conditions, the maximum

25 Kuroshio intrusion flux reached more than twice that before the typhoon.

26 **Plain Language Summary** Typhoons passing through the Kuroshio region have an important impact on the

27 Kuroshio intrusion into the South China Sea. Although the effects of monsoons, sea surface pressure gradients,

28 mesoscale eddies, β effects, ENSO, PDO and other factors on the Kuroshio intrusion are well understood, the

29 influence of typhoons on the Kuroshio current is not clear. This paper uses the COAWST coupling model to assess

30 the impact of typhoons on the Kuroshio axis and the impact of the Kuroshio intrusion on the South China Sea.

31   Under typhoon conditions, the Kuroshio intrusion is the strongest in the subsurface layer. The studied typhoon

32   yields significant increases in water, heat, and salt fluxes from the Kuroshio intrusion into the South China Sea,

33   and the contribution of the typhoon to these fluxes is as high as approximately 40%. Typhoons have an important

34   impact on Luzon transport.

35   1 Preface

36   The South China Sea is the largest marginal sea in the Western Pacific. The region has a tropical monsoon

37   climate, with northeast winds prevailing in winter and southwest winds prevailing in summer. The deep-sea basin

38   of the South China Sea is mainly composed of the Dongshan Islands in the northeast, the Xisha Islands in the

39   northwest, the Zhongsha Islands in the middle, the Huangyan Islands in the east, and the Nansha Islands in the

40   south. The South China Sea is connected to the East China Sea by the Taiwan Strait in the north. In the south, the

41   Luzon Strait is connected to the Pacific Ocean, and the Mindoro Strait and the Balabac Strait are connected to the

42   Sulu Sea. The Karimata Strait is connected to the Java Sea in the south. The Strait of Malacca is connected to the

43   Andaman Sea in the Indian Ocean. The Luzon Strait lies between Taiwan Island and Luzon Island and plays an

44   important role in water transport and dynamic interactions between the South China Sea and the Western Pacific.

45   The water transport between the Western Pacific and the South China Sea displays a "sandwich structure" in the

46   vertical direction (Chen & Huang, 1996; Qu, 2002; Yuan, 2002; Tian et al., 2006; Yuan et al., 2014; Gan et al.,

47   2016). The Western Pacific water enters the South China Sea from the surface and bottom layers and flows out of

48   the South China Sea from the middle layer. The South China Sea circulation is cyclonic circulation in the upper

49   and bottom layers and anticyclonic circulation in the middle layer. The interannual variability in the surface and

50   subsurface salinity levels in the South China Sea is affected by the intensity of the Kuroshio intrusion. Zeng et al.

51   (2014) suggested that the surface water desalination in the South China Sea in 2012 was caused by a large

52   freshwater input and the weakening of the Kuroshio intrusion. After 2012, the salinization of seawater above 150

53   m was mainly due to the decrease in evaporation and the increase in the Kuroshio intrusion (Zeng et al., 2018).

54   Nan et al. (2016) found that the salinity of the South China Sea above a depth of 100 m decreased at a rate of

55   -0.012 yr^{-1} from 1993 to 2012, and desalination was most obvious on the west side of the Luzon Strait; additionally,

56   it was suggested that desalination was related to the weakening of the Kuroshio intrusion. Chen et al. (2019) found

57   that the surface salinization of the entire South China Sea from 2016 to 2017 extended from the subsurface layer in

58   the northeastern part of the South China Sea to the southwestern part of the South China Sea and believed that this

59 was related to the intensified Kuroshio intrusion. Li et al. (2015) analyzed Argo data and concluded that the

60 salinity of the Pacific Ocean increased above 200 m between 2005 and 2015, which may have impacted the

61 salinity in the northeastern South China Sea through transport via the Luzon Strait. In addition, the mesoscale

62 eddies and circulations in the South China Sea are affected by the Kuroshio intrusion; when the Kuroshio current

63 intrudes into the South China Sea, there is a maximum velocity layer between 40-70 m in the subsurface layer. The

64 conversion of strong baroclinic pressure causes the mesoscale eddy in the northeastern South China Sea to become

65 more active. This maximum velocity layer is a bridge connecting the Kuroshio and the mesoscale eddy in the

66 South China Sea (Wang et al., 2020). Li et al. (2015) suggested that the water in the Western Pacific affects the

67 South China Sea in the form of mesoscale eddies in summer, and in autumn, this water intrudes and affects the

68 South China Sea in the form of land slope currents. Shu et al. (2016, 2019) and Liu et al. (2019) analyzed

69 temperature and salinity data obtained by underwater gliders in the South China Sea and concluded that the

70 captured anticyclonic eddies, with notably different from temperatures and salinities than the rest of the South

71 China Sea, were associated with the Kuroshio. Additionally, water transport in the Luzon Strait can transmit

72 ENSO signals to the South China Sea (Qu et al., 2004).

73   The Kuroshio is the northward branch of the North Equatorial Current (NEC) on the east side of Luzon Island.

74 This current is characterized by strong flow velocities, large flows, a narrow flow range, high temperatures and

75 high salinities and is one of the most important ocean currents in the world. As an important part of Luzon Strait

76 Transport (LST), the Kuroshio intrusion has an important impact on the South China Sea. The Kuroshio intrusion

77 is affected by many factors, such as monsoons, sea surface pressure gradients, mesoscale eddies, β effects, sea

78 surface temperature gradients, ENSO, PDO, and typhoons. Farris and Wimbush (1996) found that the Kuroshio

79 can intrude into the South China Sea only when the southerly component of the ground wind stress is greater than

80 0.08 N·m^{-2} and that local wind stress has an important influence on the path of the Kuroshio in the Luzon Strait.

81 Yuan (2002) suggested that water transport in the Luzon Strait caused by monsoons only occurs at the surface,

82 with westward movement in winter and eastward movement in summer. Kuehl and Sheremet (2009) also

83 confirmed through laboratory experiments that the Ekman transport caused by wind stress determines the angle

84 and flux of the Kuroshio intrusion into the South China Sea. Hsin et al. (2012) used a numerical model to quantify

85 the effect of the East Asian monsoon on LSTs. The results indicated that the annual average LST at 120.75°E is

86 -4.0±5.1 Sv and that the intrusion direction is westward. If the East Asian monsoon influence is excluded, the

87 annual average LST is approximately 4 Sv, and the intrusion direction is eastward. However, some studies have

88 indicated that the amount of water transport due to wind stress is small compared to that associated with the

89 Kuroshio intrusion and that the pressure gradient caused by monsoons is most important for water transport in the

90 Luzon Strait (Qu et al., 2004; Nan et al., 2013). The accumulation of seawater caused by the East Asian monsoon

91 creates a sea surface pressure gradient between the Western Pacific and the South China Sea, which has an

92 important impact on water transport via the Luzon Strait (Metzger & Hurlburt, 1996). In the Pacific Ocean from

93 20°N-25°N, mesoscale eddies propagate westward, and up to 60% of the eddies in the Western Pacific that intrude

94 into the South China Sea through the Kuroshio current (Zheng et al., 2011). When an eddy reaches the western

95 boundary of the Pacific, it interacts with the western boundary current; the western boundary current blocks the

96 westward propagation of the eddy, and the eddy changes the intensity and path of the western boundary current.

97 The cyclonic eddies weaken the Kuroshio intrusion, and anticyclonic eddies enhance the Kuroshio intrusion (Lien

98 et al., 2014). Lien et al. (2014) suggested that the intensity of the Kuroshio intrusion into the South China Sea is

99 closely related to the local sea level anomaly (SLA) gradient. An anticyclonic eddy can increase the SLA gradient

100 and enhance the Kuroshio intrusion into the South China Sea. Conversely, an cyclonic eddy reduces the SLA

101 gradient and weakens the Kuroshio intrusion into the South China Sea. Qian et al. (2018) showed that the

102 anticyclonic eddy on the east side of the Kuroshio axis can change the Kuroshio intrusion flow pattern in the

103 Luzon Strait from a gap flow state to an intrusion state with a shedding eddy. Yuan (2002) used a balance equation

104 $f\frac{dw}{dz} = \beta v$ (where f is the Coriolis force parameter, z is the vertical coordinate, v and w are the meridional and

105 vertical velocities, and β is the meridional gradient of f) and found that the components accounted for most of the

106 water transport volume; therefore, the β effect is a crucial dynamic mechanism for the generation of the Kuroshio

107 current loop. A sea surface pressure gradient promotes the generation of current loops, and the β effect can

108 increase the strength of the Kuroshio current loops. If there is no β effect, the LST will be greatly reduced, and the

109 circulation of the South China Sea will change. Additionally, the strength of the Kuroshio intrusion on the east side

110 of the Luzon Strait is directly related to the strength of intrusion into the South China Sea. Research by Yaremchuk

111 and Qu (2004) showed that when the Kuroshio current is small (10 Sv) in November and December, the Kuroshio

112 is likely to intrude into the South China Sea. When the Kuroshio current is large, inertia influences that the western

113 boundary current flows across gaps, and the intensity of the Kuroshio intrusion is small. ENSO and PDO affect the

114 intensity of the Kuroshio intrusion by influencing the north-south movement of the NEC bifurcation position

115 (Yuan et al. al., 2014; Wu, 2013). When PDO is in the warm phase, the corresponding oscillation plays a leading

116 role in the north-south movement of the NEC bifurcation position, and the role of ENSO is not obvious. When

117 PDO is in the cold phase, ENSO plays a leading role in the north-south movement of the NEC bifurcation position,

118 and PDO plays a small role.

119   The Western Pacific is a typhoon-prone area. Typhoons passing through the Kuroshio area will have an

120 important impact on the Kuroshio intrusion into the South China Sea. Hsu et al. (2018) believed that when the

121 rotating wind speed of a typhoon coincides with the direction of the main velocity of the Kuroshio current, the

122 Kuroshio current speed increases, and vice versa. Tada et al. (2018) studied the impact of typhoons on the

123 Kuroshio axis near Japan and believed that typhoons cause significant changes in the Kuroshio axis. Most of the

124 Kuroshio axis turns counterclockwise, which promotes northward flow near the coast. Kuo et al. (2011) found that

125 after a typhoon, the ocean temperature near the Luzon Strait significantly decreases, and the decrease in

126 temperature is greater than that east of Luzon Island. Hsu and Ho (2019) analyzed underwater glider observation

127 data and found that a typhoon in the Kuroshio area near Taiwan will cause the temperature of the subsurface

128 seawater to increase and the salinity of the subsurface water to decrease. Lü et al. (2021) found that the super

129 typhoon Soudelor caused the thermocline to rise and the thickness of the thermocline to increase, which led to the

130 reverse intrusion of the Kuroshio tributaries into the continental shelf of the East China Sea. Although many

131 intrusion-related processes are well understood, the effects of typhoons on the Kuroshio intrusion are still

132 relatively unclear. This paper selects a typical typhoon that moves north along the axis of the Kuroshio and uses

133 the COAWST coupling model to assess the impact of the typhoon on the Kuroshio axis and the impact of the

134 Kuroshio intrusion on the South China Sea. Section 2 describes the selected typhoon, the COAWST coupling

135 model verified by measurement data and the main research objectives. Section 3 analyzes the impact of the

136 typhoon on the Kuroshio axis, the influence of the Kuroshio intrusion on the water, heat, and salt fluxes in the

137 South China Sea, and the impact of the Kuroshio intrusion on the temperature and salinity in the South China Sea

138 after the typhoon passes. Section 4 provides a discussion and conclusions.

139 ## 2 Introduction to the data methods and models

140 ### 2.1 Typhoon information and research area

141   This article focuses on Typhoon No. 1506, called the "Hongxia" typhoon, which started as a tropical storm

142 (TS) in the Northwest Pacific (9.4°N/140.7°E) at 18:00 on May 3, 2015 (Universal Time, as used throughout the

143 paper). Hongxia moved westward in the initial stage. At the beginning of the formation of Hongxia, it was located

144 at the weak point of the subtropical high; it moved relatively slowly, and the vertical wind shear increased, which

145 was not conducive to typhoon development. However, the high sea surface temperature of 28-29°C in the

146 Northwest Pacific maintained and increased the intensity of red clouds. At 14:00 on May 6, the direction of

147 movement changed to northwest and west. After reaching typhoon (TY) and strong typhoon (STY) statuses, the

148 position of Hongxia was close to the axis of the Kuroshio current at 12:00 on May 9, and the sea surface

149 temperature east of Luzon reached above 30°C, which provided energy for Hongxia and promoted its evolution

150 into a super typhoon (super TY). At 00:00 on May 11, due to the friction of the Luzon terrain, the status of

151 Hongxia on the east side of the Luzon Strait changed from a super TY to an STY, and the system moved northeast

152 to east. At 06:00 on May 11, the status of Hongxia on the east side of the southernmost tip of Taiwan Island

153 weakened from an STY to a TY, and the system moved northeastward. At 00:00 on May 12, Hongxia weakened

154 into a severe tropical storm. Hongxia landed in Japan that day, leading to considerable precipitation. The specific

155 information for Typhoon Hongxia is shown in Table 1. The typhoon path and the main research area in this paper

156 are shown in Figure 1.

157

Table 1. Information for Typhoon "Hongxia"

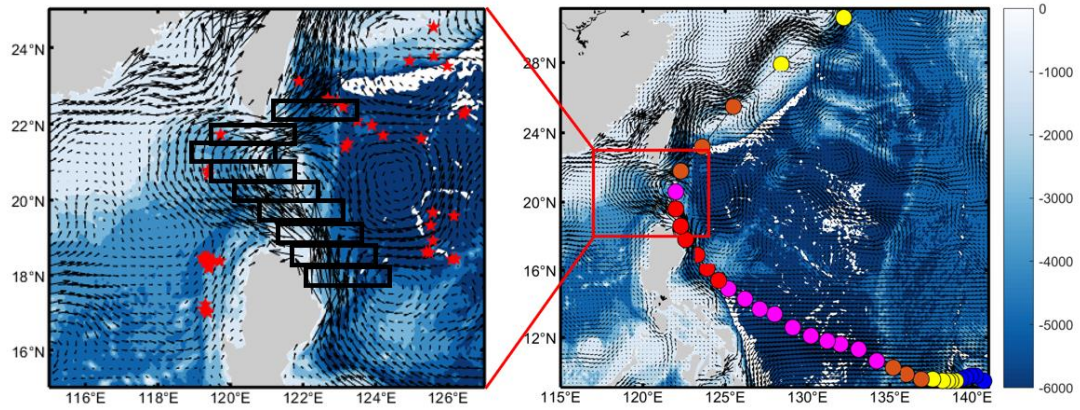| Date	Central location	Central pressure (hPa)	Maximum wind speed (m/s)	Wind direction	Intensity
05-03 18:00	9.4N/140.7E	998	18	W	TS
05-05 00:00	9.4N/139.0E	990	25	W	STS
05-06 06:00	9.5N/136.9E	975	33	WNW	TY
05-07 00:00	10.6N/134.2E	955	42	WNW	STY
05-09 12:00	15.4N/124.6E	935	52	NW	Super TY
05-11 00:00	20.6N/122.0E	950	45	ENE	STY
05-11 06:00	21.8N/122.3E	960	40	NE	TY
05-12 00:00	27.9N/128.4E	980	30	NE	STS

158

Figure 1. Schematic diagram of the path of Typhoon Hongxia and the main research area (the color of the base

map indicates the water depth, which is taken from ETOPO2; the black arrow indicates the monthly average

surface geostrophic current velocity in May 2015; the red five-pointed stars are used to denote the Mass Argo buoy

positions; the black rectangular frame is used to show the axis of the Kuroshio current; the red line segments are

18.5°N and 21°N; colored dots indicate the center position and intensity of the typhoon).

2.2 COAWST model introduction and verification

The regional coupled ocean-atmosphere-wave numerical model describes the typhoon motion processes at

three different temporal and spatial scales and the different physical properties of the mesoscale atmosphere, ocean,

and sea surface waves in three dimensions. Both the atmosphere and the ocean are fluid systems on Earth, and

their motion is governed by the control equation for Earth fluid motion. Ocean waves are small-scale waves that

occur at the sea-air interface, and their motion follows the law of the development and propagation of waves. The

numerical model used in this paper to study the ocean-atmosphere-wave interactions during a typhoon is the

ocean-atmosphere-wave-sediment transport COAWST model system (Warner et al., 2010, 2012). The COAWST

coupled modeling system uses a mature numerical model and advanced modeling technology, including ocean,

atmosphere, ocean wave, sediment transport modules and couplers.

In recent years, relevant scholars have evaluated and analyzed the typhoon simulation capabilities of the

COAWST model. Research has shown that the COAWST model can effectively simulate the typhoon movement

direction and intensity changes in the fully coupled state. Overall, the simulation results of the COAWST model

for typhoon processes are in good agreement with observed data (Warner et al., 2010, 2012; Liu et al., 2015).

The WRF has 29 floors vertically, with a horizontal resolution of 9 km. The parameterization schemes

selected were the WSM3 microphysics scheme, the RRTM longwave radiation and Dudhia shortwave radiation

180   scheme, the MM5 similar theoretical surface layer scheme, the YSU planetary boundary layer scheme, and the

181   Kain-Fritsch cumulus convection scheme. ROMS has a horizontal resolution of 9 km, 20 layers vertically, a

182   surface stretch coefficient of 4.0, and a bottom stretch coefficient of 0.1; additionally, a GLS parameterized scheme

183   is used for vertical mixing. The SWAN model uses the same grid as ROMS, and the roughness is based on the

184   Taylor and Yelland parameterization scheme. The grid weight interpolation among models is based on the SCRIP

185   toolkit. The initial field and boundary value field of the atmospheric model use NCEP FNL reanalysis data with a

186   temporal resolution of 4 h and a spatial (horizontal) resolution of 1°×1°. Assimilation data with a 0.083°×0.083°

187   resolution from HYCOM are used for the initial and boundary fields of the ocean, and ETOPO1 is used for the

188   terrain data. The integral DT is 60 s in the model, and the coupled exchange DT is 600 s.

189   Before and after the typhoon, 42 buoy profile data series obtained near the Luzon Strait (shown in Figure 1

190   with the red five-pointed stars) were compared with the model data from the same locations and simulated at the

191   same times to verify the credibility of the model data. A comparison of the results suggests that the model data are

192   consistent with the measured buoy profiles. The temperature error is basically controlled in the range of 1.0 ℃,

193   and the salinity error is generally within 0.1 (Figure 2). The mean square error of temperature is 1.029 ℃, and the

194   mean square error of salinity is 0.011. Figure 3 shows a comparison of the sea surface temperature (SST) of the

195   model and the optimal interpolated sea surface temperature (OISST) of NOAA before and after the typhoon on

196   May 6 and May 14, respectively. Figure 3c and f show the differences between the two datasets. The mode SST

197   and OISST differences are basically controlled within 0.5 ℃; only near the northeastern part of Taiwan Island and

198   the south side of the Ryukyu Islands is the difference comparatively large. Therefore, the model data and the

199   measured data are consistent, and the quality of the simulated pattern data is sufficient.
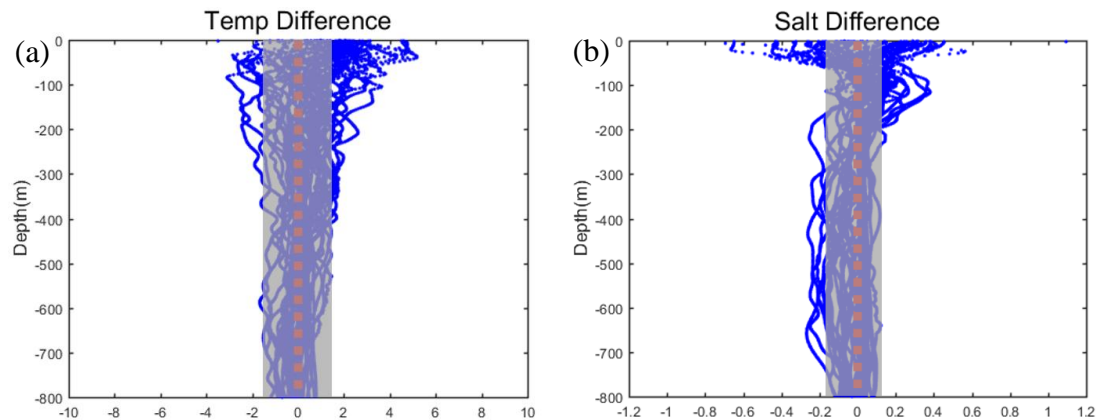

200   Figure 2. (a) Temperature error and (b) salinity error of the model data based on buoy data verification (shadows
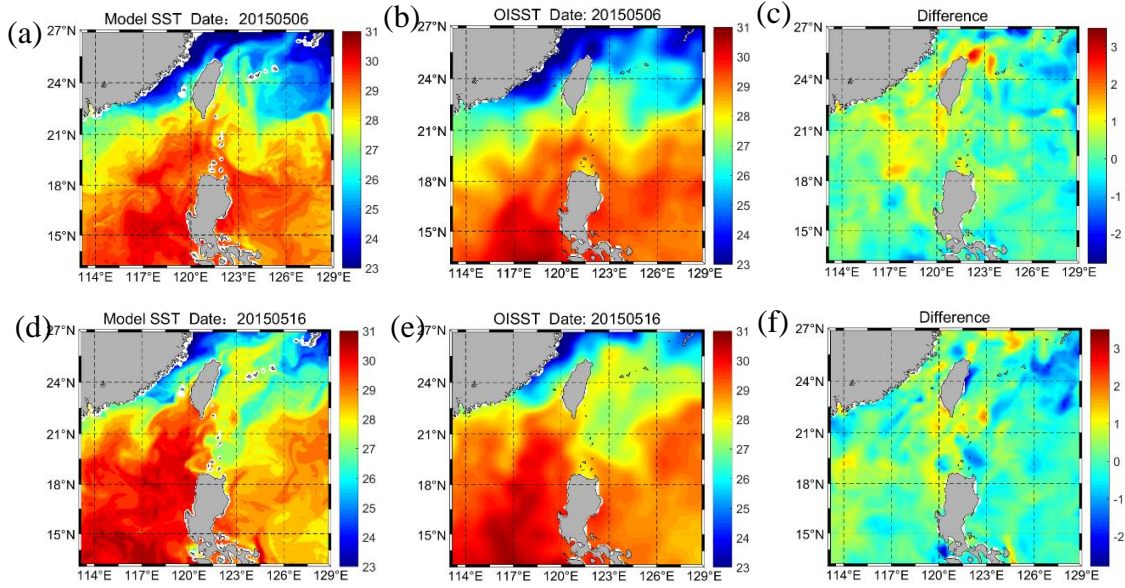
201   represent the mean square errors)

Figure 3. Comparison of model SST and optimal interpolated SST (the first row indicates pretyphoon; the second row represents post-typhoon; the first column represents model data; the second column represents satellite remote sensing data; the third column represents the difference between the two)

Typhoon Hongxia formed on May 4, 2015. The simulation period in this paper starts at 00:00 on May 3, 2015, runs 75 days, and ends at 00:00 on July 17, 2015. The model range is 12-27.5 °N and 112.5-129.0 °E, the grid horizontal resolution is 9 km, and the number of grids is 180×180. The model results are output every 6 h. The vertical stratification is divided into 20 layers, and the stratification in areas with a water depth greater than 1000 m includes layers at 2.2 m, 6.8 m, 12.2 m, 18.7 m, 26.9 m, 37.6 m, 51.5 m, 69.4 m, 92.0 m, 119.5 m, 151.8 m, 188.8 m, 230.9 m, 279.5 m, 336.8 m, 406.2 m, 491.6 m, 598.1 m, 731.7 m, and 900.0 m. There are 301 output results for each layer.

3 Results

3.1 The impact of typhoons on the Kuroshio axis

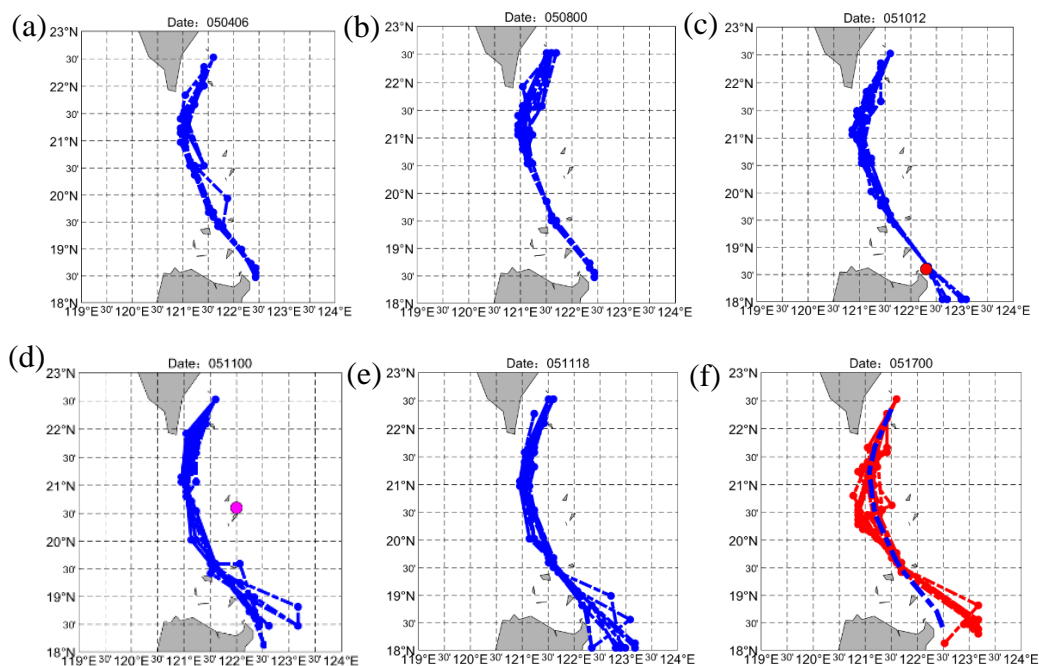### 3.1.1 The impact of typhoons on the position of the Kuroshio axis

Figure 4 shows the changes in the position of the Kuroshio axis over 500 m before and after the studied typhoon passes. The latitudes of 18-22.5°N are evenly divided into 9 segments (18-18.5°N, 18.5-19°N, 19-19.5°N, 19.5-20°N, 20-20.5°N, 20.5-21°N, 21-21.5°N, 21.5-22°N, and 22-22.5°N, as shown in the black rectangular frame in Figure 1), and the position of the maximum flow velocity in each section is defined as the position of the Kuroshio axis in the section. The colored dots in the picture indicate the location of the typhoon, and the color

220 indicates the intensity (as shown in Figure 1).

221   From May 5 to May 11, there was an anticyclonic eddy on the right side of the Kuroshio current, and it

222 continuously merged into the Kuroshio axis with high-velocity seawater. At this time, the eddy influenced the

223 speed of the Kuroshio, and then the intensity of the anticyclonic eddy rapidly weakened. Eventually, the eddy

224 completely merged into the Kuroshio current and disappeared. Figure 4a-e show that when the anticyclonic eddy

225 has a considerable influence on the Kuroshio current velocity and that the position of the Kuroshio axis minimally

226 changes; thus, the influence of the anticyclonic eddy on the position of the Kuroshio axis is negligible. By

227 comparing the distribution of Kuroshio axis at different times, we find that the axis began to move slightly

228 westward on approximately May 17, and the amplitude of the westward movement then gradually increased. The

229 range of the westward movement reached a maximum on May 31st. Near 21°N, the axis of the Kuroshio bent the

230 most toward the South China Sea, and the intrusion position is the westernmost of those observed. Seven days

231 after the typhoon passed, the axis of the Kuroshio began to shift toward the South China Sea by approximately

232 0.25° (Figure 4f). Eleven days after the typhoon passed, the axis of the Kuroshio deviated by approximately 0.5°

233 (Figure 4g). Seventeen days after the typhoon passed, the axis of the Kuroshio deviated by approximately 0.75°

234 (Figure 4h). Twenty days after the typhoon passed, the Kuroshio axis shifted by approximately 1° (Figure 4i).

235   The change in the position of the Kuroshio axis can effectively reflect the Kuroshio intrusion. Because only

236 the position of the maximum velocity of the Kuroshio is considered, the actual scope of the impact of the Kuroshio

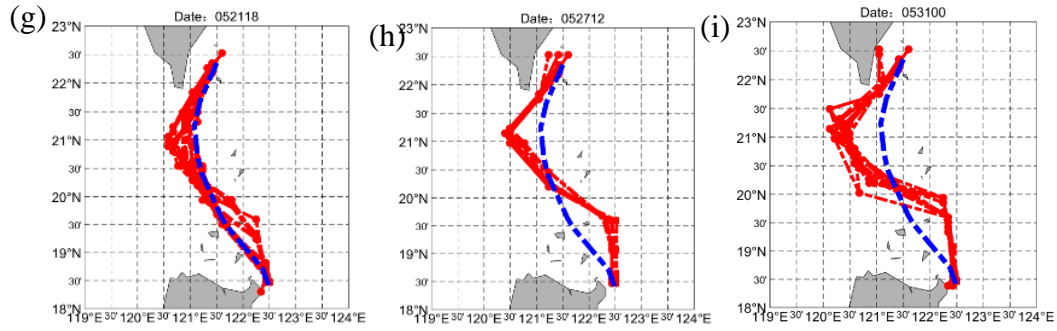237 current on the South China Sea should be broad.

238 Figure 4. Changes in the position of the main Kuroshio axis before and after the typhoon ((a-e) Before the typhoon

239 passes; (f-i) After the typhoon passes. The blue dotted line indicates the average position of the main axis before

240 the typhoon passes).

241 3.1.2 The impact of typhoons on the velocity of the Kuroshio axis

242 In this paper, two sections are selected at 18.5°N and 21°N on the Kuroshio axis to study the velocity changes

243 at various depths before and after the typhoon passes.

244 At 11:00 on May 10, the typhoon center passed the Kuroshio axis. An analysis of the Kuroshio axis velocity

245 in the 18.5°N section (Figure 5a) yielded the following results: (1) Before the typhoon passed, the Kuroshio axis

246 surface velocity was approximately 1 m/s, and the velocity at 200 m was approximately 0.6 m/s. (2) When the

247 typhoon center passed through this section on May 10, the Kuroshio current speed increased sharply. Seven hours

248 after the typhoon center passed, the velocity in each layer reached a maximum, and the surface velocity was as

249 high as 2.5 m/s, which was twice as high as the velocity before the typhoon. The velocity distribution generally

250 maintained a decreasing trend from shallow to deep. (3) After the velocity reached the maximum value, it began to

251 rapidly decrease. After 24 h of typhoon conditions, the velocity reached a minimum, and the velocity in each layer

252 of the Kuroshio decreased to 0.6 m/s. (4) After the typhoon, the velocity in each layer exhibited a certain

253 downward trend. On May 16, the velocity in each layer of the Kuroshio was reduced to half of the velocity before

254 the typhoon (except for a slight rebound after reaching a minimum). (5) At approximately 12:00 on May 16, the

255 velocity began to rise, and at 12:00 on May 19, the velocity returned to the state observed before the typhoon.

256 At 02:00 on May 11, the center of the typhoon was approximately 100 km to the east of the Kuroshio axis. An

257 analysis of the Kuroshio axis velocity in the 21°N section (Figure 5b) indicated that (1) under normal conditions,

258 the Kuroshio surface velocity is approximately 1.15 m/s, and the velocity at 200 m is approximately 0.7 m/s. In

259 general, the velocity decreases from the sea surface to lower layers. (2) The velocity gradually increased beginning

260   on May 5 and reached a maximum value at approximately 00:00 on May 9. (3) After the velocity above 100 m

261   reached a maximum, the effect of the typhoon to the east became notable, and the velocity magnitude oscillated; a

262   significant downward trend after May 19 was observed. (4) The velocity below 100 m reached a maximum and

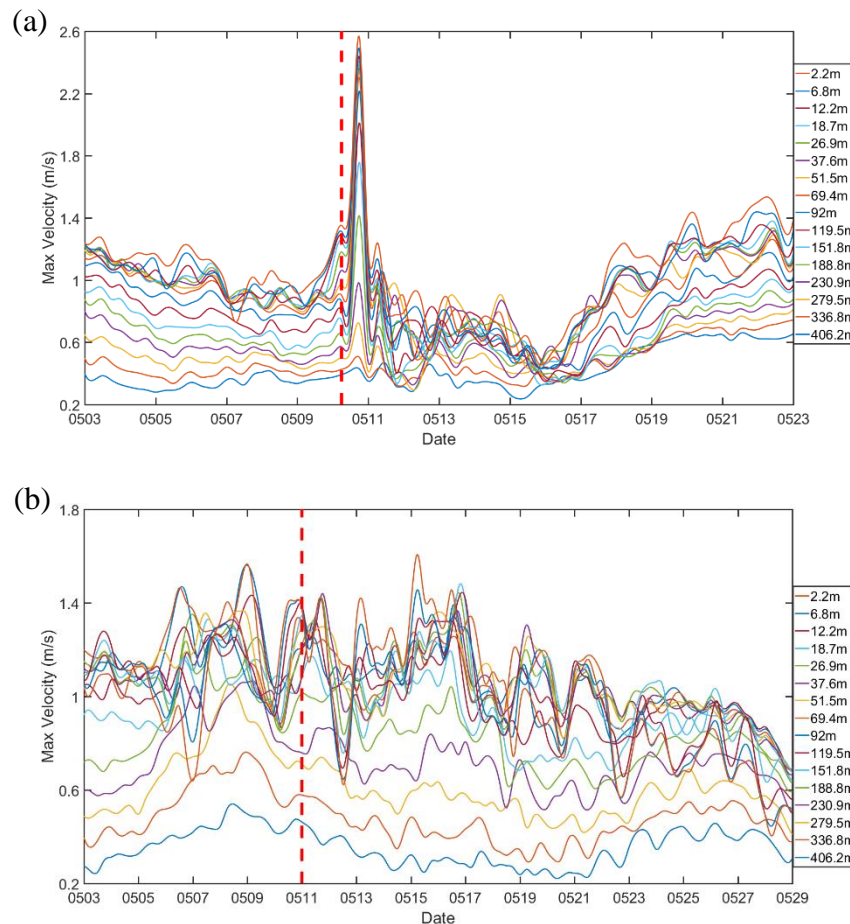263   then gradually decreased and returned to normal on May 19.

264   Figure 5. Variations in the Kuroshio main axis velocity before and after the typhoon passes ((a) 18.5°N sectional

265   velocity; (b) 21°N sectional velocity. The red dashed line indicates the time when the typhoon passed).

266   In summary, when the typhoon center passed through the Kuroshio axis, the strong wind speed caused the

267   ocean velocity to increase sharply, and the velocity reached a maximum 7 h after the typhoon passed; this value is

268   as high as twice the velocity before the typhoon. After the typhoon passed, a strong disturbance to the ocean

269   remained, and it hindered the northward flow of the Kuroshio. After the typhoon passed, the velocity of the

270   Kuroshio exhibited a downward trend, and the velocity decreased to a minimum approximately 6 d after the

271   typhoon passed. The flow rate returned to normal after 3 d.

272   In the middle of the Luzon Strait, the speed of the Kuroshio from May 5 to May 9 exhibited an increasing

273   trend. At this time, the typhoon had just formed and had not yet affected the Kuroshio axis. According to the

274 analysis of the velocity field (Figure 6), a westwardly moving anticyclonic eddy formed on the right side of the

275 Kuroshio. When approaching the Kuroshio axis, the northward current at the western boundary of the eddy

276 continuously merged into the Kuroshio axis and followed the Kuroshio to higher latitudes. The speed of the eddy

277 was greater than the speed of the Kuroshio, the Kuroshio continued to absorb the anticyclonic eddy, and the

278 velocity near the Kuroshio axis increased. The seawater at the outer boundary of the anticyclonic eddy merged into

279 the Kuroshio in sequential layers, the intensity of the anticyclonic eddy continued to weaken, and the speed of the

280 Kuroshio gradually recovered. On approximately May 18, the anticyclonic eddy was basically absorbed by the

281 Kuroshio current. The increase in velocity in this section was mainly due to the influx of anticyclonic eddies.
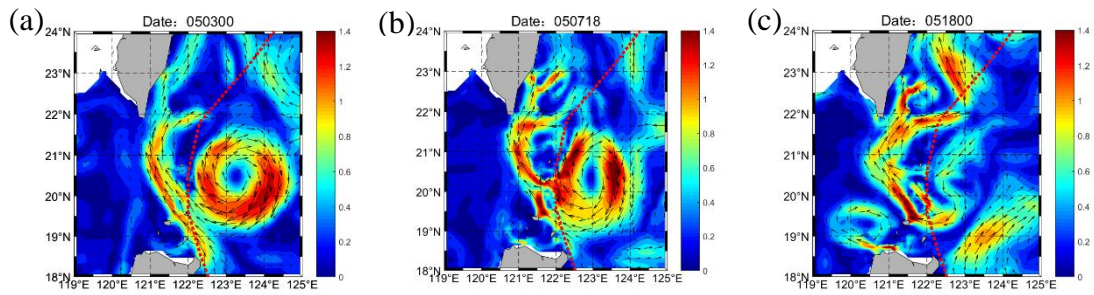

282 Figure 6. Plane distribution of velocity when the anticyclonic vortex approached the Kuroshio axis (taking a water

283 depth of 119.5 m as an example; the red dotted line indicates the typhoon path).

284 3.1.3 The impact of typhoons on the water flux of the Kuroshio intrusion into the

285 South China Sea

286 The 121°E section is selected to calculate the water flux Q that the Kuroshio transports to the South China

287 Sea over 400 m. This calculation is as follows (Cai et al., 2002; Fang & Wang, 2002):

$$Q = \sum_i v_{ni} A_i \tag{1}$$

288 where v_{ni} is the normal velocity component passing through the ith grid in the section and A_i is the area of

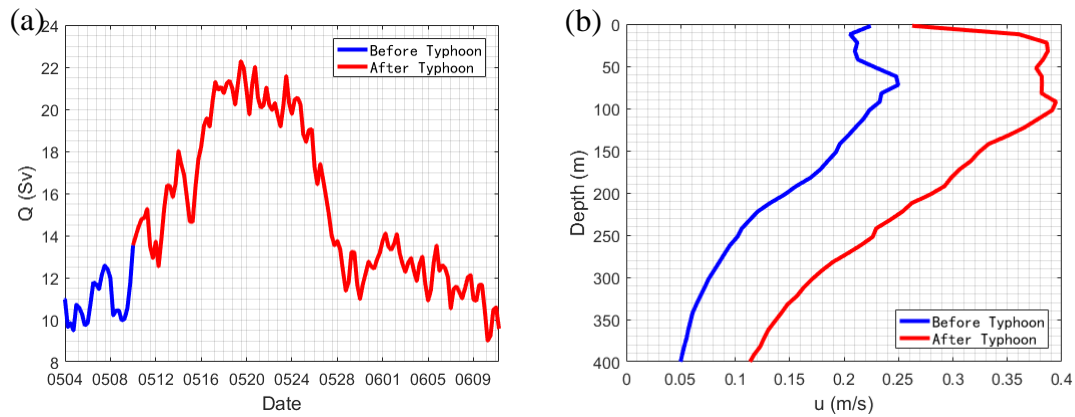289 the grid. The units of the water flux are 1 Sv=$1 \times 10^6 \, \mathrm{m}^3$/s.

Figure 7. (a) The change in the water flux of the Kuroshio to the South China Sea above 400 m; (b) The average westward velocity u in each depth layer at 121°E (the blue line represents the pretyphoon case; the red line represents the post-typhoon case).

In Figure 7a, the blue line indicates the water flux of the Kuroshio into the South China Sea before the typhoon passes, and the red line shows the Kuroshio intrusion when the typhoon reaches the Luzon Strait and after the typhoon passes. As shown in the figures, after the typhoon reached the Luzon Strait, the water flux of the Kuroshio intrusion into the South China Sea increased rapidly. The Kuroshio intrusion reached its maximum approximately 6 d after the typhoon, and the maximum flux was 22 Sv, which was twice as high as that before the typhoon. The strongest intrusion state lasted for a week, and the amount of intrusion displayed a downward trend. Approximately 25 d after the typhoon passed, the intrusion flux returned to the state observed before the typhoon.

Figure 7b shows the change in the average westward velocity with depth at 121°E before and after the typhoon passed. As shown in the figures, after the typhoon passed, the westward velocity above 400 m increased, and the most obvious influence was observed at 20-100 m, indicating that the impact of the typhoon on the Kuroshio intrusion was most significant in subsurface layers. As depth increased, the influence of the typhoon on the velocity gradually decreased.

The water flux of the Kuroshio intrusion into the South China Sea at different water depths before and after the typhoon was calculated, and the corresponding typhoon contribution was determined. Table 2 indicates that above 400 m, the total water flux of the Kuroshio into the South China Sea before the typhoon was 10.96 Sv, and after the typhoon, this value reached 18.33 Sv; overall, the typhoon contribution to the flux was as high as 40.2%. Above 600 m, the contribution of the typhoon to the flux is as high as 40.7%. Under typhoon conditions, the largest increase in the flux of the Kuroshio intrusion into the South China Sea occurs in the 20-400 m layer. The increase gradually decreases with water depth, but the contribution of the typhoon is still significant. The increase

312 in the surface water flux is smaller than that for subsurface water. In addition, the average water flux from 0-400 m

313 during the 10-year period of 2008-2017 is calculated as a reference. The water flux before the typhoon was close to

314 the water flux under the background climatic state, and the water flux after the typhoon increased significantly.

315 Table 2. Comparison of water flux before and after the typhoon (Unit: Sv)

	0-20m	20-200m	200-400m	0-400m	0-600m	0-400m (ten-year average)[a]
Pre-typhoon	0.89	7.07	3	10.96	12.54	
Post-typhoon	1.23	11.7	5.41	18.33	21.15	7.86
Typhoon contribution rate	27.60%	39.60%	44.50%	40.20%	40.70%	

316 a: data from CMEMS

317 3.1.4 The impact of typhoons on the temperature and salt fluxes of the Kuroshio

318 intrusion into the South China Sea

319 The 121°E section is selected to calculate the heat flux H and the salt flux S transported by the Kuroshio into

320 the South China Sea at 400 m. These fluxes are calculated as follows (Cai et al., 2002; Fang & Wang, 2002):

$$H = \sum_i T_i \rho_i \, C_p v_{ni} A_i \tag{2}$$

$$S = \sum_i s_i \rho_i \, v_{ni} A_i \tag{3}$$

321 where T_i is the temperature in the ith grid, ρ_i is the density of the grid, C_p is the specific heat capacity of

322 seawater at constant pressure, and s_i is the salinity in the ith grid. The units of the heat flux are 1 J/s= 1 W and 1

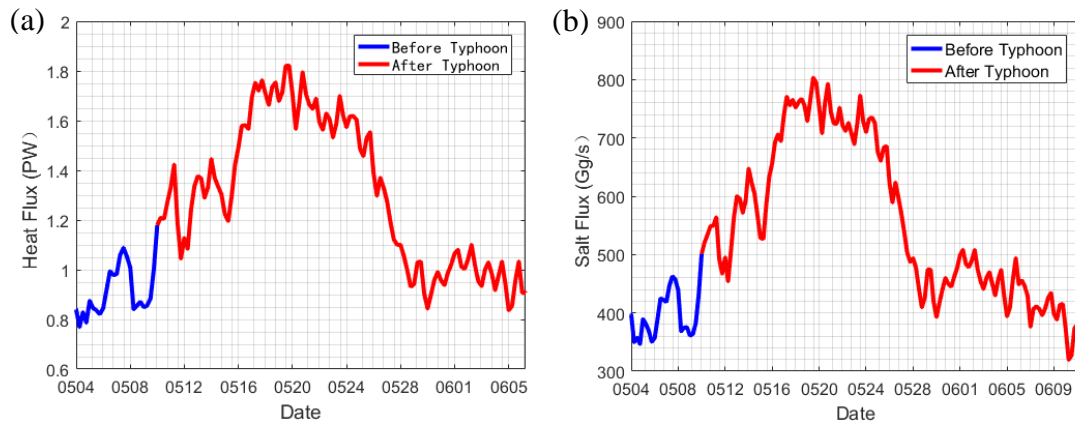323 PW=1×10^{15} W. The units of the salt flux are 1 g/s=1 Gg/s =1×10^9 g/s.

324 Figure 8. (a) Heat and (b) salt flux variations associated with the Kuroshio before and after the typhoon intruded

325 into the South China Sea (the blue line indicates the pretyphoon case; the red line indicates the post-typhoon case)

326   In Figures 8a and b, the blue line denotes the heat and salt fluxes of the Kuroshio intrusion into the South

327   China Sea before the typhoon, and the red line is the Kuroshio intrusion when the typhoon reaches the Luzon Strait

328   and after the typhoon. The heat and salt fluxes reaches a maximum approximately 6 d after the typhoon, and the

329   maximum can reach 1.8 PW and 800 Gg/s, which is more than twice that before the typhoon. The maximum

330   amount of intrusion began to decrease after approximately a week, and the corresponding state returned to the

331   original intrusion state 25 d after the typhoon.

332   The heat and salt fluxes of the Kuroshio intrusion into the South China Sea at different water depths before

333   and after the typhoon were calculated, and the typhoon contribution to these fluxes was calculated. From Tables 3

334   and 4, above 400 m, the heat flux and salt fluxes of the Kuroshio intrusion the South China Sea before the typhoon

335   are 0.892 PW and 389.15 Gg/s, and they can reach 1.473 PW and 651.46 Gg/s after the typhoon. The contributions

336   of the typhoon to these fluxes are 39.4% and 40.3%, respectively; above 600 m, the contributions of the typhoon

337   are 39.8% and 40.7%, respectively. Under typhoon conditions, the largest increase in the heat and salt fluxes

338   associated with the Kuroshio intrusion into the South China Sea is at 20-400 m. The increases in the surface heat

339   and salt fluxes are smaller than those in subsurface layers. The average heat and salt fluxes from 0-400 m during

340   the 10-year period of 2008-2017 are calculated as a reference. The heat and salt fluxes before the typhoon are

341   relatively similar to the heat and salt fluxes under typical climatic conditions, and they increase significantly after

342   the typhoon.

343   Table 3. Comparison of the heat flux before and after the typhoon (Unit: PW)

	0-20m	20-200m	200-400m	0-400m	0-600m	0-400m (ten-year average)[b]
Pre-typhoon	0.1	0.63	0.16	0.89	0.95	
Post-typhoon	0.14	1.03	0.3	1.47	1.57	0.63
Typhoon contribution rate	28.60%	38.80%	46.70%	39.50%	39.80%	

344   b: data from CMEMS

345   Table 4. Comparison of the salt flux before and after the typhoon (Unit: Gg/s)

	0-20m	20-200m	200-400m	0-400m	0-600m	0-400m (ten-year average)[c]
Pre-typhoon	32	252	106	389	445	
Post-typhoon	43	417	192	651	751	278
Typhoon contribution rate	25.60%	39.60%	42.40%	40.20%	40.70%	

346 c: data from CMEMS

3.2 The influence of the Kuroshio current on the salinity of the northeastern South China Sea after the typhoon

The typhoon caused the Kuroshio axis to bend toward the South China Sea, and the Kuroshio intrusion into the South China Sea increased the water, heat, and salt fluxes, thus influencing the salinity in the South China Sea, especially in the northeastern region. The salinities of the Western Pacific Ocean and the South China Sea are quite different, and the degree of intrusion of the Kuroshio into the South China Sea can be intuitively determined by analyzing the changes in salinity. Before the typhoon passed, the axis of the Kuroshio was relatively stable, and the salinity in the northeastern part of the South China Sea was relatively stable. Taking a water depth of 18.7 m as an example, 7 d after the typhoon passed, the axis of the Kuroshio began to bend toward the South China Sea, and the input of high-salinity water into the South China Sea increased significantly (Figure 9b). Twelve days after the typhoon passed, the Kuroshio water intruded into the South China Sea to approximately 119°E, and the impact of the intrusion on the salinity in the northeastern part of the South China Sea expanded (Figure 9c).
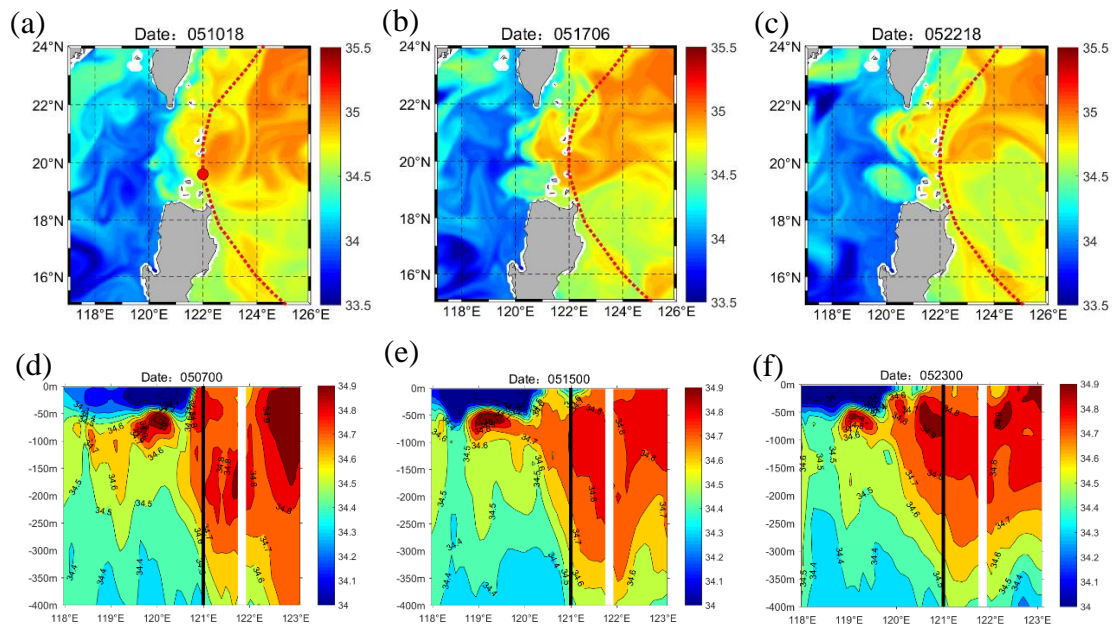

Figure 9. (a-c) Distribution of the Kuroshio input of high-salinity water into the South China Sea (taking a depth of 18.7 m as an example); (d-f) Changes in salinity in the 21°N section (blank areas in the figures are land; the black solid line indicates 121°E).

The extent of the Kuroshio intrusion into the South China Sea is most significant at 21°N (see Figure 4). The 21°N section is selected to study the impact of the typhoon on the Kuroshio intrusion into the South China Sea.

364   May 11 is the day on which the typhoon passed through the 21°N section. Figures 9d-f show the salinity changes

365   in the 21°N section before and after the typhoon passed. West of 121°E is the main low-salinity region in the South

366   China Sea, and east of 121°E is the high-salinity region of the Kuroshio. Four days after the typhoon passed,

367   high-salinity Kuroshio water intruded into the South China Sea, especially above 150 m, and the Kuroshio

368   intrusion was stronger in the subsurface layer than in the surface layer (Figure 9e). On May 23, the high-salinity

369   Kuroshio water extended to 120° E (Figure 9f).

370   To clearly analyze the impact of typhoons on the Kuroshio intrusion into the South China Sea, the average

371   salinity in each layer in the western region of the Luzon Strait (118°E-121°E, 19°N-22°N) was taken as the

372   characteristic value, and the variations in salinity over time were used to reflect the extent of the Kuroshio

373   intrusion into the South China Sea. Figure 10 shows that the salinity of each layer increased to varying degrees

374   after the typhoon passed on May 11, reflecting the influence of the typhoon on the Kuroshio intrusion into the

375   South China Sea at different depths.

376   After the typhoon passed, the salinity at 12.2 m changed by approximately 0.06, indicating that the typhoon

377   strengthened the Kuroshio intrusion at the surface of the South China Sea. However, the increase in salinity above

378   10 m was smaller than that near 20 m. Combined with the southwestern summer monsoon in the South China Sea,

379   it is speculated that the low-salinity water near the surface in the southern South China Sea accumulates in the

380   northeast due to the effect of the predominant wind field, resulting in less obvious changes in surface salinity in the

381   northeastern South China Sea than in subsurface layers. The salinity of subsurface water increased the most under

382   typhoon conditions. The salinity values of 26.9 m, 37.6 m, and 51.5 m increased at rates of 0.013 /d, 0.012 /d, and

383   0.016 /d, respectively, reflecting the impact of the typhoon on the Kuroshio intrusion. The impact is most obvious

384   in subsurface layers, and this result is consistent with the conclusion drawn in Figure 9. The increase in salinity

385   below 100 m decreases with depth (not shown in the figure), indicating that the impact of typhoons on the

386   Kuroshio intrusion gradually decreases below 100 m.

387   Even after the typhoon passed, the Kuroshio water intrusion into the South China Sea was strengthened.

388   However, Figure 4 shows that the axis of the Kuroshio only bends toward the South China Sea a week after the

389   typhoon passes. Since the determination of the Kuroshio axis in Figure 4 is based on the maximum velocity within

390   the observed range, the salty water at the western boundary of the Kuroshio had already begun to intrude into the

391   South China Sea when the axis position remained almost unchanged, and the change in the axis position lagged.

392 The Kuroshio intrusion into the South China Sea was mainly reflected in the surface and subsurface layers and had

393 a significant impact on the salinity above the subsurface layer in the northeastern part of the South China Sea. This

394 result corresponds to the changes in the surface and subsurface salinity levels in the South China Sea in recent

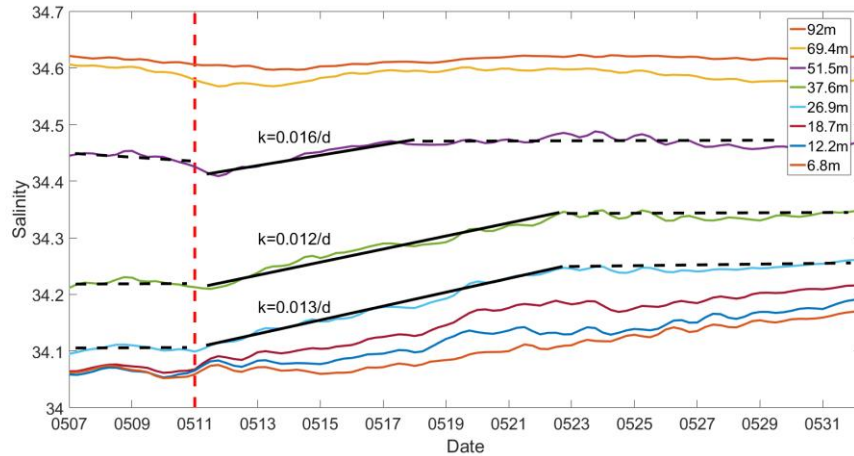395 decades, which are often related to the Kuroshio intrusion (Zeng et al., 2014; Nan et al., 2016; Chen et al., 2019; Li

396 et al., 2015).

397

398 Figure 10. The average salinity change in each layer above 100 m in the northeastern part of the South China Sea

399 (the black line segment represents the fitting result; the red dotted line represents the typhoon transit time)

400 ## 3.3 The influence of the Kuroshio current on the temperature in the northeastern

401 ## South China Sea after the typhoon

402 We further analyzed the temperature changes in the northeastern part of the South China Sea and studied the

403 impact of hot Kuroshio water on the South China Sea after the typhoon. Figure 11a shows the temperature

404 distribution around the Luzon Strait before the typhoon passed, and Figures 11b and c show the temperature

405 distribution around the Luzon Strait after the typhoon. The results indicate that after the typhoon passed, the hot

406 Kuroshio water gradually intruded into the South China Sea. Based on Figures 4 and 6, the temperature increase

407 on the southern side of Taiwan Island is caused by the shift in the Kuroshio axis to the South China Sea, and the

408 temperature increase on the northwest side of Luzon Island is caused by the anticyclonic vortex that the Kuroshio

409 shed in the South China Sea. Figure 11d-f correspond to the temperature section at 21°N. The results show that

410 after the typhoon passed, the hot Kuroshio water obviously intruded into the South China Sea near 121°E.

411 In the northeastern part of the South China Sea (118°E-121°E, 19°N-22°N), the average temperature at

412 different times is used as a characteristic value to reflect the influence of the Kuroshio intrusion on the temperature

413   in the South China Sea. After the typhoon passed, the temperatures at depths of 151.8 m, 188.8 m, and 230.9 m

414   increased at rates of 0.033 °C/d, 0.042 °C/d, and 0.042 °C/d, respectively, indicating that the influence of the

415   Kuroshio intrusion on the temperature in the South China Sea was most significant in subsurface layers (Figure

416   12b). From May 12-15, the temperatures in the 26.9 m, 37.6 m, 51.5 m, and 69.4 m layers decreased at rates of

417   0.092°C/d, 0.154°C/d, 0.169°C/d, and 0.154°C/d, respectively; notably, the typhoon caused a general decrease in

418   the upper-layer temperature of the Kuroshio current, which indirectly caused a decrease in the average temperature

419   in the northeastern part of the South China Sea (Figure 12a).
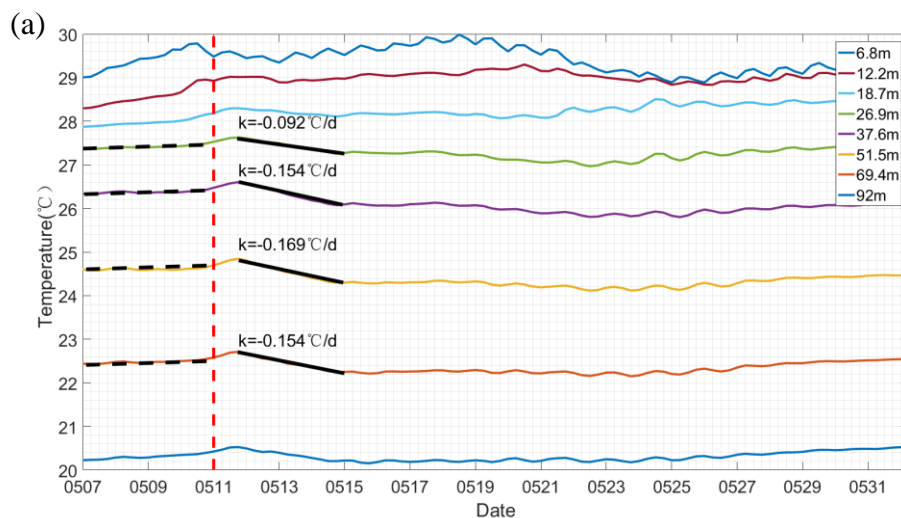

420   Figure 11. (a-c) Distribution of the Kuroshio input of hot water into the South China Sea (with a depth of 18.7 m as

421   an example); (d-f) Changes in salinity in the 21°N section (blank areas in the figures are land, and the black solid
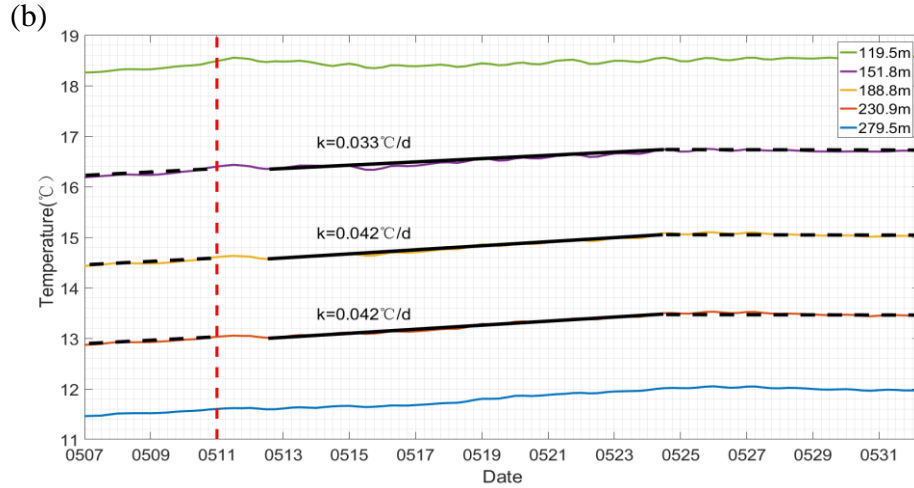
422   line indicates 121°E).

(b)

4 Discussion and summary

427 Our preliminary research suggests that typhoons that moved along the right side of the Kuroshio path and

428 across the northern part of Luzon had a significant impact on the Kuroshio intrusion into the South China Sea. The

429 increase in the water flux under typhoon conditions above 400 m was approximately $1.27\times10^{13}\,\mathrm{m}^3$ and 3.31×10^{12}

430 m^3 along these two paths, respectively. Additionally, the increase in the heat flux under typhoon conditions above

431 400 m was approximately 1.00×10^{21} J and 6.48×10^{20} J, and the increase in the salt flux under typhoon conditions

432 above 400 m was approximately 4.53×10^{17} g and 3.15×10^{17} g. Thirteen typhoons followed each of these two paths

433 in the ten years from 2008 to 2017, and the water, heat and salt fluxes associated with the Kuroshio intrusion

434 caused by typhoons above 400 m in the ten years were approximately $2.08\times10^{14}\,\mathrm{m}^3$, $2.14\times10^{22}\,\mathrm{J}$, and $9.98\times10^{18}\,\mathrm{g}$,

435 accounting for 8.4%, 10.8%, and 11.4% of the total water, heat, and salt fluxes, respectively. Studying the impact

436 of typhoons on the Kuroshio intrusion is important in analyses of Luzon transport.

437 By comparing the results of this paper with the water fluxes in the Luzon Strait obtained by previous authors

438 (Table 5), we find that the net water fluxes before the typhoon obtained in this paper are similar to those reported

439 by Zhou et al. (2009) and Yuan et al. (2012). The westward net water flux is smaller than the results based on the

440 ADCP observations of Tian et al. (2006). The eastward water flux is basically consistent with the results obtained

441 by Yang et al. (2011) based on ADCP observations, although the westward water flux obtained in this study is

442 larger than that previously reported. The direction of the net water flux is opposite that reported by Yang et al.

443　(2010). After a typhoon, the water flux will increase substantially. Generally, the water flux in the Luzon Strait is

444　affected by factors such as season and depth, and the data accuracy and calculation method can influence results.

445　Thus, there are some differences in the calculated results.

446　　Table 5. Comparison of water flux values reported in the Luzon Strait (a positive value represents eastward, unit:
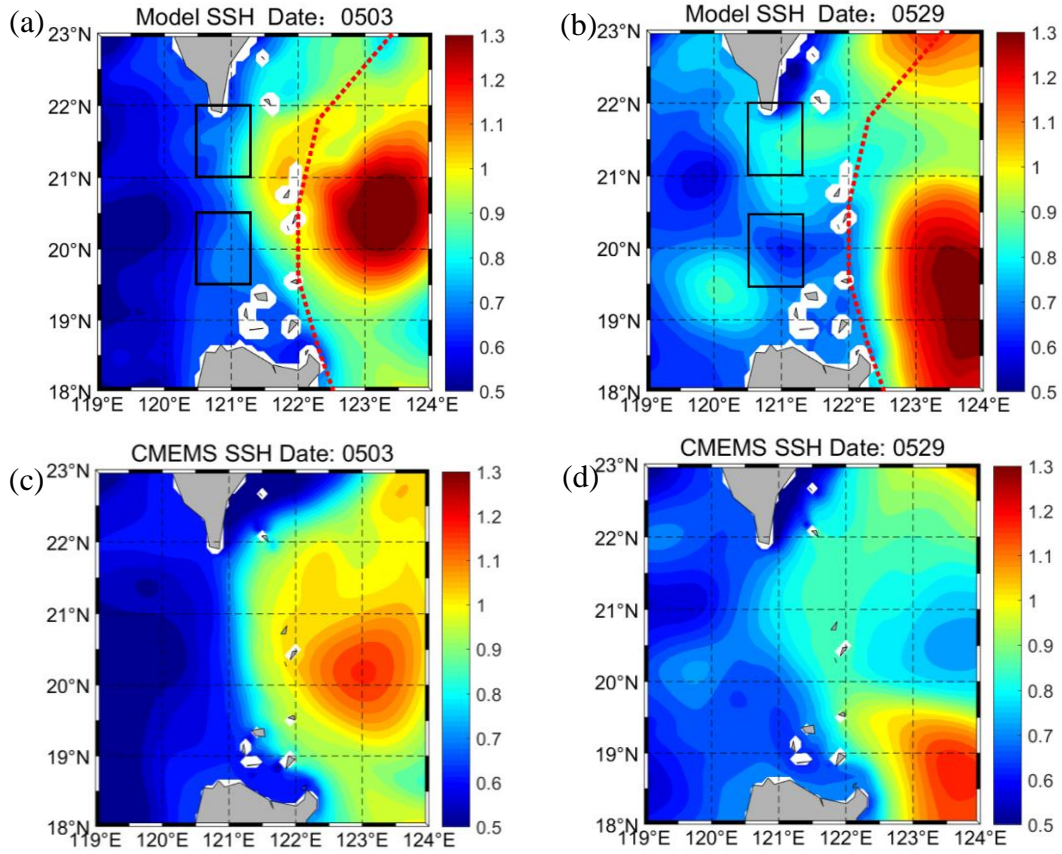
447　　　　　　　　　　　　　　　　　　　　　　　　Sv)

Source	West	Esat	Net	Depth Range	Period	Method
This study	-12.54	9.90	-2.64	0~600m	May.2015 (before typhoon)	COAWST Model
This study	-21.15	17.79	-3.36	0~600m	May.2015 (after typhoon)	COAWST Model
Tian et al. (2006)	\	\	-9	0~500m	Oct.2005	ADCP
Zhou et al. (2009)	\	\	-4.47	0~500m	Sep.2006	Dynamic method
Yang et al. (2010)	\	\	5.0	0~500m	Jul.2007	ADCP
Yang et al. (2011)	-2.4	10.5	7.9	about 0~600 m	Aug.2008	ADCP
Yuan et al. (2012)	\	\	-2.66	0~500m	Apr.2008	Dynamic method

448　　　　Under typhoon conditions, the intensity of the Kuroshio intrusion into the South China Sea is affected by

449　various mechanisms. In the Luzon Strait, the center of the typhoon is located to the east of the Kuroshio axis, and

450　northerly winds act on this axis. With the geostrophic current formula (Equation 4), we calculated the average

451　geostrophic current velocity before and after the typhoon (Figures 13a and b). The results show that the

452　geostrophic current velocities before and after the typhoon were 0.076 m/s and 0.141 m/s, respectively. The

453　geostrophic current velocity after the typhoon was twice that before the typhoon, and all current directions are west.

454　As shown in Figure 7b, the westward velocity in the surface layer before the typhoon was approximately 0.22 m/s.

455　The sea level difference caused by the typhoon increased the velocity of the geostrophic current by 0.065 m/s, and

456　this effect was considerable. We believe that after the typhoon, northerly winds hindered the northward flow of the

457　Kuroshio, causing the Kuroshio water to accumulate in the northern part of the Luzon Strait, and the sea level in

458　the northern part of the Luzon Strait became higher than that in the southern part of the Luzon Strait. The

459　difference in sea surface pressure in the north-south direction produced a westward geostrophic current, and the

460　intensity of the Kuroshio intrusion into the South China Sea increased.

$$u = -\frac{1}{\rho f}\frac{\partial p}{\partial y} \tag{4}$$

461   In addition, when the typhoon passed through the Luzon Strait, its center was located to the right of the

462   Kuroshio axis. The northerly wind at the western boundary of the typhoon center influenced the Kuroshio axis (as

463   shown in Figure 14). A northerly wind can produce westward Ekman transport and strengthen the Kuroshio

464   intrusion into the South China Sea. Furthermore, near the Luzon Strait, the strong disturbance to the ocean after

465   the typhoon caused the northern component of the Kuroshio current to continue to decrease (as shown in Figure

466   13e). According to the balance $f\frac{dw}{dz} = \beta v$, when the western boundary current is weak and dominated by the β

467   vorticity term, the western boundary current intrudes into the strait, and a large anticyclonic bend forms. The

468   Kuroshio current in the Luzon Strait shifts from a gap flow pattern to an intrusive flow pattern, and the Kuroshio
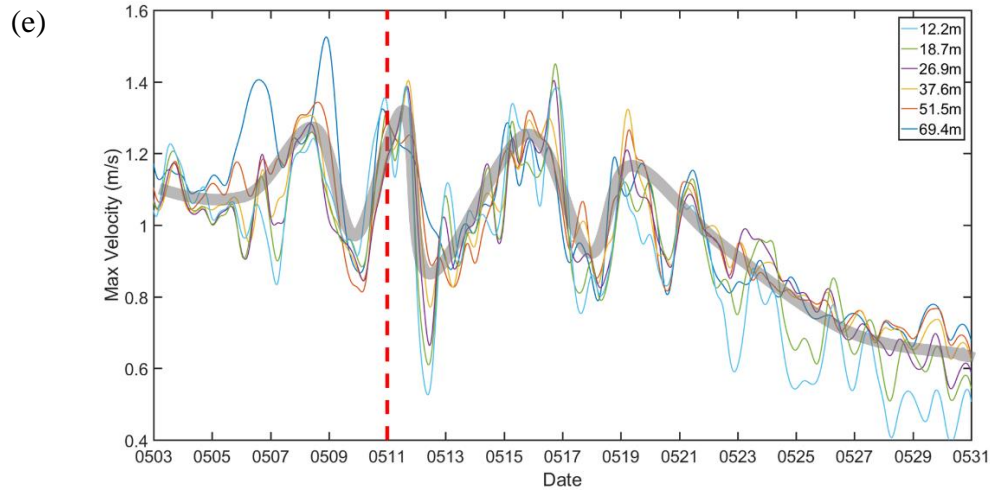
469   intrusion is strengthened.

(e)

Figure 13. (a-d) Sea level changes near the Luzon Strait before and after the typhoon; (e) The northerly component

variation diagram for the Kuroshio current in the 21°N section before and after the typhoon (The black box is the

range selected to calculate the geostrophic current velocity. (a) and (b) are based on model data; (c) and (d) are

based on the CMEMS reanalysis data for comparison with the model data. The black dotted line indicates the

fitting result; the red dotted line indicates the typhoon transit time).
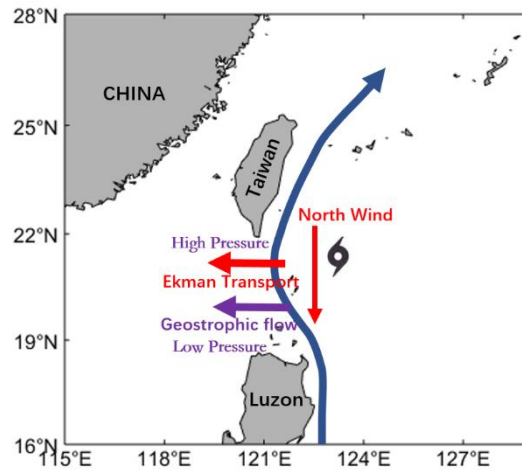

Figure 14. Ekman transport and geostrophic current velocities under typhoon conditions (the west-pointing red

arrow indicates the Ekman transport caused by wind stress; the west-pointing purple arrow indicates the

geostrophic current caused by the difference in sea surface pressure between north and south).

(1) When typhoon "Hongxia" passed, in the latitude direction, the Kuroshio intrusion into the South China

Sea was the most significant at 21°N. In the vertical direction, the Kuroshio intrusion was strongest in the

subsurface layer, leading to the most significant changes in temperature and salinity in the northeastern part of the

South China Sea occurring in subsurface layers. The westward deviation of the Kuroshio axis caused by the

483 typhoon displayed a certain lag compared with the hot and salty water intrusion into the South China Sea

484 approximately 7 d later. The impact of the typhoon on the Kuroshio intrusion into the South China Sea lasted for

485 20 d. The typhoon increased the water, heat, and salt fluxes associated with the Kuroshio intrusion into the South

486 China Sea, and the contribution of the typhoon to these fluxes was as high as 40%. Under typhoon conditions, the

487 maximum Kuroshio intrusion flux reached more than twice that before the typhoon.

488   (2) The north-south sea surface pressure gradient caused by the typhoon produced a westward geostrophic

489 current. The geostrophic current after the typhoon was twice as high as that before the typhoon, and it increased

490 the intensity of the Kuroshio intrusion into the South China Sea. The northerly wind associated with the typhoon

491 resulted in westward Ekman transport, which strengthened the Kuroshio intrusion into the South China Sea.

492   (3) From 2008 to 2017, typhoons that had a significant impact on the Kuroshio intrusion of water, heat, and

493 salinity fluxes above 400 m, reaching approximately 2.08×10^{14} m^3, 2.14×10^{22} J, and 9.98×10^{18} g and accounting

494 for 8.4%, 10.8%, and 11.4% of the total water, heat, and salt fluxes, respectively, during this ten-year period. Thus,

495 typhoons have an important impact on Luzon transport.

501

References

Cai, S. Q., Liu, H. L., & Li, W. (2002). Water Transport Exchange Between the South China Sea and Its Adjacent Seas. *Advances in Marine Science*, 20 (3), 29-34.

Chen, C., & Huang, M. H. (1996). A mid-depth front separating the South China Sea water and the Philippine sea water. *Journal of Oceanography*, 52(1), 17-25. https://doi.org/10.1007/BF02236530

Chen, X., Liu, Z., Wang, H., Xu, D., & Wang, L. (2019). Significant salinity increase in subsurface waters of the South China Sea during 2016–2017. *Acta Oceanologica Sinica*, 38(11), 51-61. https://doi.org/10.1007/s13131-019-1498-z

Fang, G., Wei, Z., & Wang, K., et al. (2002). Inter-regional water, heat and salt transport in China's offshore waters: results of the global variable grid model. *Science China (Series D)*, 32(12), 967-977.

Farris, A., & Wimbush, M. (1996). Wind-Induced Kuroshio Intrusion into the South China Sea. *Journal of Oceanography*, 52(6), 771-784. https://doi.org/10.1007/BF02239465

Gan, J., Liu, Z., & Hui, C. (2016). A three-layer alternating spinning circulation in the South China Sea. *Journal of Physical Oceanography*, 46(8), 2309-2315. https://doi.org/10.1175/JPO-D-16-0044.1

Hsin Y, Wu C, Chao S. (2012). An updated examination of the Luzon Strait transport. *Journal of Geophysical Research Oceans*, 117(C3).

Hsu, P. C., & Ho, C. R. (2019). Typhoon-induced ocean subsurface variations from glider data in the Kuroshio region adjacent to Taiwan. *Journal of Oceanography*, 75(1), 1-21. https://doi.org/10.1007/s10872-018-0480-2

Hsu, T. W., Chou, M. H., Hou, T. H., & Liang, S. J. (2018). Typhoon effect on Kuroshio and Green Island wake: a modelling study. *Ocean ence Discussions*, 12(6), 3199-3233. https://doi.org/10.5194/osd-12-3199-2015

Kuehl, J. J, & Sheremet, V. A. (2009). Identification of a cusp catastrophe in a gap-leaping western boundary current. *Journal of Marine Research*, 67(1), 25-42. https://doi.org/10.1357/002224009788597908

Kuo, Y. C., Zheng, Z. W., & Zheng Q., et al. (2011). Typhoon-Kuroshio interaction in an air-sea coupled system: Case study of Typhoon Nanmadol. *Ocean Modelling*, 2018.

Li, D., Zhou. M., Zhang Z., Zhong, Y., Zhu, Y., & Yang, C., et al. (2015). Intrusions of Kuroshio and Shelf Waters on Northern Slope of South China Sea in Summer 2015. *Journal of Ocean University of China*, 17(3), 477-486. https://doi.org/10.1007/s11802-018-3384-2

Lien, R. C., Cheng, Y. H., Ho, C. R., Qiu, B., & Lee, C. M., et al. (2014). Modulation of Kuroshio transport by mesoscale eddies at the Luzon Strait entrance. *Journal of Geophysical Research: Oceans*, 119(4), 2129-2142. https://doi.org/10.1002/2013JC009548

Liu, N., Ling T., Wang, H., Zhang, Y., & Gao, Z. (2015). Numerical Simulation of Typhoon Muifa(2011) Using a Coupled Ocean-Atmosphere-Wave-Sediment Transport(COAWST) Modeling System. *Journal of Ocean University of China*, 14(2):199-209. https://doi.org/10.1007/s11802-015-2415-5

Liu, Z., Chen, X., Yu, J., Xu, D., & Sun, C. (2019). Kuroshio intrusion into the South China Sea with an anticyclonic eddy: evidence from underwater glider observation. *Journal of Oceanology and Limnology*, 37(5), 1469-1480. https://doi.org/10.1007/s00343-019-8290-y

Lü, H., Liu, Y., Wang, Y., Cui, Y., Ge, X., & Zhou, L. et al. (2021). Abnormal reverse intrusion of the Kuroshio Branch Current induced by super typhoon soudelor. *Estuarine, Coastal and Shelf Science,* 256. https://doi.org/10.1016/j.ecss.2021.107377.

Metzger, E. J., & Hurlburt, H. E. (1996). Coupled dynamics of the South China Sea, the Sulu Sea, and the Pacific Ocean. *Journal of Geophysical Research: Oceans*, 101(C5), 12331-12352. https://doi.org/10.1029/95JC03861

Nan, F., Xue. H., Chai, F., Wang, D., Yu, F., & Shi, M., et al. (2013). Weakening of the Kuroshio Intrusion into the South China Sea over the Past Two Decades. *Journal of Climate*, 26(20), 8097-8110. https://doi.org/10.1175/JCLI-D-12-00315.1

Nan, F., Yu, F., Xue, H., Zheng, L., & Wang, D. (2016). Freshening of the upper ocean in the South China Sea since the early 1990s. *Deep Sea Research Part I: Oceanographic Research Papers*, 118, 20-29. https://doi.org/10.1016/j.dsr.2016.10.010

Qian, S., Wei, H., Xiao, J., & Nie, H. (2018). Impacts of the Kuroshio intrusion on the two eddies in the northern South China Sea in late spring 2016. *Ocean Dynamics*, 68(12), 1695-1709. https://doi.org/10.1007/s10236-018-1224-y

Qu, T. (2002). Evidence for water exchange between the South China Sea and the Pacific Ocean through the Luzon Strait. *Acta Oceanol. Sin.*, 21(2), 175-185.

Qu, T., Kim, Y. Y., Yaremchuk, M., Tozuka, T., Ishida, A., & Yamagata, T. (2004). Can Luzon Strait transport play a role in conveying theimpact of ENSO to the South China Sea? Journal of Climate, 17(18), 3644–3657. https://doi.org/10.1175/1520-0442(2004)017<3644:CLSTPA>2.0.CO;2

Shu, Y. Q., Xiu, P., Xue H., Yao, J., & Yu, J. (2016). Glider-observed anticyclonic eddy in northern South China

559   Sea. *Aquatic Ecosystem Health & Management*, 19(3), 233-241.
560   https://doi.org/10.1080/14634988.2016.1208028

561 Shu, Y., Chen, J., Li, S., Wang, Q., Yu, J., & Wang, D. (2019). Field-observation for an anticyclonic mesoscale
562   eddy consisted of twelve gliders and sixty-two expendable probes in the northern South China Sea during
563   summer 2017. *Scientia Sinica(Terrae)*, 62(2), 451-458. https://doi.org/10.1007/s11430-018-9239-0

564 Tada, H., Uchiyama, Y., & Masunaga, E. (2018). Impacts of two super typhoons on the Kuroshio and marginal
565   seas on the Pacific coast of Japan. *Deep Sea Research*, 132(FEB.), 80-93.
566   https://doi.org/10.1016/j.dsr.2017.12.007

567 Tian, J., Yang, Q., Liang X, Xie, L., Hu, D., & Fan, W., et al. (2006). Observation of Luzon Strait transport.
568   *Geophysical Research Letters*, 33(19). https://doi.org/10.1029/2006GL026272

569 Wang, Q., Zeng, L., Chen, J., He, Y., Zhou, W., & Wang, D. (2020). The linkage of Kuroshio intrusion and
570   mesoscale eddy variability in the northern South China Sea: Subsurface speed maxìmum. *Geophysical
571   Research Letters*, 47(11). https://doi. org/10.1029/2020GL087034

572 Warner, J. C., Armstrong, B. N., He, R., Zambon, J. B., Olabarrieta, M., & Voulgaris, G., et al. (2012).
573   Development and applications of a Coupled-Ocean-Atmosphere-Wave-Sediment Transport (COAWST)
574   Modeling System. *AGU Fall Meeting Abstracts*, 230-244. https://doi.org/ 10.1016/j.ocemod.2010.07.010

575 Warner, J. C., Armstrong, B., He, R., & Zambon, J. B. (2010). Development of a Coupled Ocean–Atmosphere–
576   Wave–Sediment Transport (COAWST) Modeling System. *Ocean Modelling*, 35(3), 230-244.
577   https://doi.org/10.1016/j.ocemod.2010.07.010

578 Wu, C. R. (2013). Interannual modulation of the Pacific Decadal Oscillation (PDO) on the low-latitude western
579   North Pacific. *Progress in Oceanography*, 110(3), 49-58. https://doi.org/10.1016/j.pocean.2012.12.001

580 Yang, Q., Tian, & Zhao, W. (2011). Observation of material fluxes through the Luzon Strait. *Chinese Journal of
581   Oceanology and Limnology*, 29(1), 26-32. https://doi.org/10.1007/s00343-011-9952-6

582 Yang, Q., Tian, J., & Zhao, W. (2010). Observation of Luzon Strait transport in summer 2007 – ScienceDirect.
583   *Deep Sea Research Part I: Oceanographic Research Papers*, 57(5), 670-676.
584   https://doi.org/10.1016/j.dsr.2010.02.004

585 Yaremchuk, M., & Qu, T. (2004). Seasonal Variability of the Large-Scale Currents near the Coast of the
586   Philippines. *Journal of Physical Oceanography*, 34(4), 844-855.
587   https://doi.org/10.1175/1520-0485(2004)034<0844:SVOTLC>2.0.CO;2

588 Yuan, D. (2002). A numerical study of the South China Sea deep circulation and its relation to the Luzon Strait
589   transport. *Acta Oceanologica Sinica*, 21(2), 187-202.

590 Yuan, D. (2002). A numerical study of the South China Sea deep circulation and its relation to the Luzon Strait
591   transport. *Acta Oceanologica Sinica*, 21(2), 187-202.

592 Yuan, Y., Liao, G., Kaneko, A., Yang, C., Zhu, X. H., & Chen, H., et al. (2012). Currents in the Luzon Strait

593   obtained from moored ADCP observations and a diagnostic calculation of circulation in spring 2008.

594   *Dynamics of Atmospheres and Oceans*, 58, 20-43. https://doi.org/10.1016/j.dynatmoce.2012.07.002.

595 Yuan, Y., Liao, G., Yang, C., Liu, Z., Hong, C., & Wang, Z. G. (2014). Summer Kuroshio Intrusion through the
596   Luzon Strait confirmed from observations and a diagnostic model in summer 2009. *Progress in
597   Oceanography*, 121(121), 44-59. https://doi.org/10.1016/j.pocean.2013.10.003

598 Yuan, Y., Yang, C., Liao, G., Chow, C. H., Liu, Z. & Zhu, X. H., et al. (2014). Variation in the Kuroshio intrusion:
599   Modeling and interpretation of observations collected around the Luzon Strait from July 2009 to March 2011.
600   *Journal of Geophysical Research: Oceans*, 119(6), 3447-3463. https://doi.org/10.1002/2013JC009776

601 Zeng, L., Chassignet, E., Schmitt, R. W., Xu, X., & Wang, D. (2018). Salinification in the South China Sea since
602   late 2012: a reversal of the freshening since 1990s. *Geophysical Research Letters*, 45(6), 2744-2751.
603   https://doi.org/10.1002/2017GL076574

604 Zeng, L., Liu, W. T., Xue, H., Peng, X., & Wang, D. (2014). Freshening in the South China Sea during 2012
605   revealed by Aquarius and in situ data. *Journal of Geophysical Research: Oceans*, 119(12), 8296-8314.

606 Zheng, Q., Tai, C. K., Hu, J., Lin, H., Zhang, R. H., & Sun, F. C., et al. (2011). Satellite altimeter observations of
607   nonlinear Rossby eddy–Kuroshio interaction at the Luzon Strait. *Journal of Oceanography*, 67(4):365.
608   https://doi.org/10.1007/s10872-011-0035-2

609 Zhou, H., Nan, F., Shi, M.C., Zhou, L.M., & Guo, P. F. (2009). Characteristics of water exchange in the Luzon

610   Strait during September 2006. *Chinese Journal of Oceanology and Limnology,* 27 (3), 650–657.

611   http://dx.doi.org/10.1007/s00343-009-9175-2.

612